Technical note

Accelerated cardiac cine MRI using locally low rank and finite difference constraints

Xin Miao [a,*], Sajan Goud Lingala [b], Yi Guo [b], Terrence Jao [b], Muhammad Usman [c], Claudia Prieto [c], Krishna S. Nayak [a,b]

[a] Department of Biomedical Engineering, University of Southern California, Los Angeles, USA
[b] Ming Hsieh Department of Electrical Engineering, University of Southern California, Los Angeles, USA
[c] Division of Imaging Sciences and Biomedical Engineering, King's College London, London, UK

ABSTRACT

Purpose: To evaluate the potential value of combining multiple constraints for highly accelerated cardiac cine MRI.
Methods: A locally low rank (LLR) constraint and a temporal finite difference (FD) constraint were combined to reconstruct cardiac cine data from highly undersampled measurements. Retrospectively undersampled 2D Cartesian reconstructions were quantitatively evaluated against fully-sampled data using normalized root mean square error, structural similarity index (SSIM) and high frequency error norm (HFEN). This method was also applied to 2D golden-angle radial real-time imaging to facilitate single breath-hold whole-heart cine (12 short-axis slices, 9–13 s single breath hold). Reconstruction was compared against state-of-the-art constrained reconstruction methods: LLR, FD, and k-t SLR.
Results: At 10 to 60 spokes/frame, LLR + FD better preserved fine structures and depicted myocardial motion with reduced spatio-temporal blurring in comparison to existing methods. LLR yielded higher SSIM ranking than FD; FD had higher HFEN ranking than LLR. LLR + FD combined the complimentary advantages of the two, and ranked the highest in all metrics for all retrospective undersampled cases. Single breath-hold multi-slice cardiac cine with prospective undersampling was enabled with in-plane spatio-temporal resolutions of 2×2 mm^2 and 40 ms.
Conclusion: Highly accelerated cardiac cine is enabled by the combination of 2D undersampling and the synergistic use of LLR and FD constraints.

1. Introduction

Cardiac cine MRI is the non-invasive gold standard technique for evaluating cardiac function and wall motion in humans [1,2]. A typical examination covers the heart using multiple 2D slices, roughly ten to twelve short-axis slices and three to six long-axis slices [1]. Scan protocols utilize electrocardiogram or plethysmo-graph gating to synchronize MRI acquisitions with the cardiac cycle, and 10–15 s breath holds to avoid artifacts from respiratory motion (one breath hold per slice). There is significant opportunity for improvement through the use of acceleration. Roughly 10% of cardiac patients have arrhythmias or are otherwise unable to hold their breath, and benefit from real-time methods that do not require cardiac synchronization or breath holding. Among appropriate patients, inconsistencies between breath holds leads to slices being acquired in different respiratory states, which requires a complex

registration step prior to quantitative functional analysis. Finally, current methods are geared towards assessment of the left ventricle, whereas assessment of the left atrium, valves, and right heart chambers requires higher and potentially isotropic spatial resolution via 3D imaging.

Several methods have been proposed to accelerate cine imaging. Parallel imaging methods shorten the scan time by exploiting the sensitivities of multiple coils [3,4]. However, high acceleration with acceleration factor above 4 is rarely used in practice because it is limited by the coil geometry and its associated g-factor SNR losses [4]. Compressed sensing (CS) has shown promise to accelerate dynamic imaging even further [5–10]. CS encourages sparse representations of the dynamic images in a known transform domain, and utilizes a non-linear recovery algorithm to reconstruct the images from undersampled k-space data. Transforms such as spatial wavelet [5,7,8], temporal frequency [7–9], and spatio-temporal finite difference [10] have been previously explored. A challenge associated with using a single sparsity constraint is the potential misfit between the model representation and the dynamic

data; many transform coefficients are often required to accurately represent the signal at hand. This limits the maximum achievable acceleration rate. Adaptive methods that rely on transforms derived from the data itself have recently been proposed. Methods based on partially separable function model (PSF) [11] that exploit similarities among pixel-time profiles include k-t PCA [12], incremented rank power factorization (IRPF) [13,14], sparsity and low rank regularization (k-t SLR) [15–17], and blind compressed sensing [18]. They all enforce a global model on every time profile being expressed as a combination of few temporal basis functions. These basis functions can be orthogonal (e.g. estimated using singular value decomposition [15–17]), or non-orthogonal (e.g. estimated via dictionary learning [18]).

Methods based on regional similarities have also been proposed. A locally low rank (LLR) scheme was proposed in [19], where low rank structure was promoted on overlapping small patches extracted from the global image matrix. k-t PCA was adapted to promote similarities on anatomically segmented compartments [20]. Motivated by the success of improving global low rank constraint via combining it with sparsity constraints [15–17,21,22], we propose to exploit additional sparsity constraints in the LLR framework. In this paper, we improve the LLR method by combining it with temporal finite difference constraint and parallel imaging, and investigate its utility for highly accelerated cardiac cine imaging.

2. Theory

2.1. Global and local low rank models

Cine images represent a time series in a complete cardiac cycle. The images can be represented as a Casorati matrix (Γ_{MxN}) by stacking the pixels from every time frame column wise, where M and N respectively represent the number of pixels per time frame, and the total number of time frames [11]. Global low rank methods (e.g. [14,15]) recover Γ from undersampled k-space data by constraining the rank of Γ as:

$$\Gamma^* = \arg\min_{\Gamma} \|F \cdot S \cdot \Gamma - m\|_2^2 + \lambda \, rank(\Gamma) \tag{1}$$

where $\boldsymbol{m}$ is the multi-coil k-space measurement, F is the Fourier undersampling operator, and S are the coil sensitivity maps.

In contrast to global low rank (GLR) methods, locally low rank (LLR) methods [19] divide the global images into patches, and enforce the low-rank constraint on the matrix of each patch:

$$\Gamma^* = \arg\min_{\Gamma} \|F \cdot S \cdot \Gamma - m\|_2^2 + \lambda \sum_{b \in \Omega} rank(C_b \Gamma) \tag{2}$$

where C_b is the operator to extract the bth patch from Γ and reform it into a Casorati matrix, and Ω is the total number of patch matrices extracted from Γ.

Compared with GLR, LLR is a more appropriate model for cardiac cine images demonstrated by Fig. 1. Fig. 1 analyzes the rank property of patch matrices extracted from a cine dataset. It can be seen from Fig. 1b that the patch matrix from the chest wall has lower effective rank than a patch extracted from the heart. Even within the heart region, the low-rank property could vary (Fig. 1c). Patch matrices from regions with more dynamics have higher effective rank.

In the previous LLR framework [19], the nuclear norm was used to relax the rank penalty, which is the closest convex approximation. Recent work has shown that using non-convex semi-norm improves the reconstruction from fewer measurements compared to the nuclear norm [15,23,24]. Here, the non-convex Schatten p-norm is used as a surrogate for the rank penalty. For a $\mathbf{M} \times \mathbf{N}$ matrix X, the Schatten p-norm is defined as:

$$\|X\|_p = \left(\sum_{i=0}^{\min(M,N)} \sigma_i^p \right)^{1/p}, p<1 \tag{3}$$

where σ_i is the i_{th} singular value of matrix X.

2.2. Combination of LLR and temporal FD

The combination of GLR with sparsity constraints has been shown in various forms to improve image recovery rate and reconstruction performance [15–17,21,22]. In this study, the LLR and temporal finite difference (FD) constraints are jointly exploited. The optimization is formulated as:

$$\Gamma^* = \arg\min_{\Gamma} \|F \cdot S \cdot \Gamma - m\|_2^2 + \lambda_{LLR}\|\Phi(\Gamma)\|_p + \lambda_{FD}\|\nabla_t(\Gamma)\|_1 \tag{4}$$

where ∇_t is the finite difference operator along time, and $\|\Phi(\Gamma)\|_p$ is the Schatten p-norm defined on patches as:

$$\|\Phi(\Gamma)\|_p = \sum_{b \in \Omega} \|C_b \Gamma\|_p, p<1 \tag{5}$$

3. Methods

Experiments were performed on both retrospectively undersampled 2D Cartesian cine data and prospectively undersampled 2D golden-angle radial data. For comparison, reconstruction on the same dataset was also performed using state-of-the-art constrained reconstruction methods. In following text, LLR, FD and LLR + FD
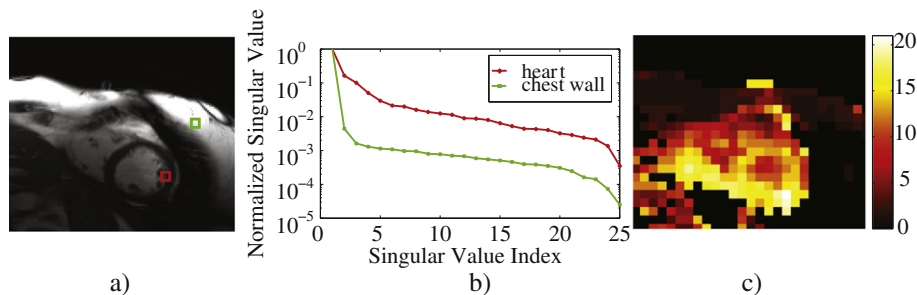
Fig. 1. Appropriateness of a locally low rank (LLR) model for cardiac cine images. (a) Reference image. Red and green boxes indicate patch matrices (size: $5 \times 5 \times N_t$) extracted from the heart region and the chest wall respectively. (b) Normalized singular values of the two matrices. It can be seen from (b) that the two matrices have significantly different levels of rank-deficiency. (c) Rank map: color indicates the rank of each patch matrix. The rank was computed as the number of singular values above 0.5% of the maximum singular value. Patches covering or partially covering the heart region of interest (ROI) have considerably higher rank than patches from the chest wall and other background tissue. Rank-deficiency also varies within the heart ROI.

would respectively refer to the reconstruction methods using the LLR constraint alone, temporal finite difference constraint alone, and the combination of both constraints.

3.1. Retrospective study

Six fully sampled cardiac cine datasets were distributed as part of the 2014 ISMRM Reconstruction Challenge [39]. The data were collected using 2D cine breath-held balanced steady state free precession (bSSFP) sequences and 32-channel cardiac receiver coils. Three of the datasets were acquired in a mid ventricular short-axis, and three at vertical long-axis. Datasets have matrix size in the range of 210×330 to 210×426, spatial resolution 1 mm^2, 30 time frames per cardiac cycle. The fully sampled datasets were retrospectively undersampled in two dimensions using variable density random [6] and Cartesian golden-angle radial sampling patterns [25–27]. Acceleration factor ranging from 5 to 30 for 2D random sampling and 10 spokes to 60 spokes per time frame for Cartesian radial sampling were chosen to evaluate the reconstruction performance of the proposed method.

The proposed method was compared against three methods, which uses the temporal FD constraint alone ($\lambda_{LLR} = 0$ in Eq. (4)), LLR constraint alone ($\lambda_{FD} = 0$ in Eq. (4)) and k-t SLR method [15]. k-t SLR was implemented by replacing the LLR constraint in Eq. (4) with global low rank constraint using Schatten p-norm [15]. For LLR constraint, overlapping square patches were extracted from the global image. Patch size was $5 \times 5 \times N_t$, which resulted in smallest normalized root mean square error (NRMSE) in the heart region. Patches were overlapped with a striding length of 2. Coil sensitivity maps were computed by averaging data from all time frames and using ESPIRIT [28]. The p-value in the Schatten p-norm computation was set as 0.5. The regularization parameters were optimized for each reconstruction method at each undersampling level by referring to normalized root mean square error (NRMSE) in the heart region. This optimization was performed for one dataset and then applied to all other datasets. In the algorithms of LLR + FD and k-t SLR, which have two regularization terms, parameters were optimized in a two dimensional version. The optimization problem in Eq. (4) was solved using an Alternating Direction Method of Multipliers (ADMM) [29]. A twice-variable-splitting technique was used to decouple the problem in Eq. (4) to simpler sub-problems that have analytical solutions [29]. The steps of the algorithm are detailed in the Appendix A. All reconstruction methods were implemented in MATLAB and executed on a 12-core Xeon workstation with 48 Gb of memory. Parallel computing was used in LLR and LLR + FD reconstructions in the step of singular value thresholding on multiple patch matrices.

For retrospective study, reconstruction results were evaluated based on both visual inspection and quantitative metrics: normalized root mean square error (NRMSE), structural similarity index (SSIM) [30] and high frequency error norm (HFEN) [31]. The choice of the three metrics was made to evaluate the reconstruction results with complimentary emphasis. NRMSE was chosen to evaluate the overall accuracy in reconstructing the spatio-temporal dynamics in the region of interest (ROI). SSIM put emphasis on image quality perception. HFEN was chosen to evaluate the fine features, edges, and spatial blurring in reconstruction. All metrics were computed within a manually segmented ROI that contained the heart. At each undersampling level, the four methods were ranked from best to worst using the quantitative metrics. Considering the variability in metric values across datasets, the ordinal ranking was averaged across all the six datasets.

- NRMSE $= \sqrt{\frac{\|\Gamma^* - \Gamma^0\|_F^2}{\|\Gamma^0\|_F^2}}$, where Γ^* is the reconstructed image, and Γ^0 is the true image.

- SSIM was computed as described in [30]. Note that 1-SSIM is presented, so that "lower is better" for all three metrics.

- HFEN $= \sqrt{\frac{\|LoG(\Gamma^*) - LoG(\Gamma^0)\|_F^2}{\|LoG(\Gamma^0)\|_F^2}}$, where LoG is a Laplacian of Gaussian filter that captures the edges. The same filter specifications as in [31] are used: kernel size of 15×15 pixels; standard deviation of 1.5 pixels.

3.2. Prospective study

A multi-slice golden-angle radial acquisition in a single breath-hold was performed on Philips 1.5 T scanner using a 32 channel cardiac coil in two healthy volunteers. Data corresponding to each slice were acquired during a single cardiac cycle with ECG triggering. Written informed consent was obtained from both subjects prior to imaging, and the protocol was approved by our institutional review board. Scan parameters were as follows: bSSFP, TR = 2.90 ms, TE = 1.45 ms, FOV: 320×320 mm^2, in-plane resolution: 2×2 mm^2, slice thickness: 8 mm, 12 slices, no inter-slice gap, number of frequency encoding points: 160, 216–272 golden angle radial profiles, and acquisition time 9–13 s. The radial profiles were retrospectively grouped into 19–20 time frames resulting in 11–13 full profiles per time frame, with a time resolution in the range of 30–40 ms. As a reference, fully-sampled cine data were acquired with Cartesian trajectory in all subjects in multiple breath holds. The reference scan used the same imaging parameters and slice geometry as the radial acquisition.

For image reconstruction, Eq. (4) was modified to include NUFFT [32] operator in place of the F operator. Coil sensitivity maps S were estimated from data using all acquired golden angle radial profiles. λ_{LLR} and λ_{FD} were empirically chosen, and were found to be different from the retrospective experiments. The optimization problem was solved using one-variable-splitting ADMM, where the step of updating the images no longer involved an analytical update, and was solved using a conjugate gradient algorithm. The rest of the implementation was the same as in the retrospective study.

4. Results

4.1. Retrospective study

The four methods (LLR + FD, LLR, FD and k-t SLR) were quantitatively compared. LLR + FD reconstruction had consistently superior NRMSE, SSIM and HFEN scores compared to the other three methods. The metric advantage of LLR + FD was more significant in cases with higher level of undersampling (Fig. 2a). The score difference for individual time frame was consistent with the average of the entire time series (Fig. 2b).

Visual observations correlated well with the quantitative evaluation. At 15 to 60 spokes per time frame, LLR + FD reconstruction better preserved fine structure such as the tricuspid valve in the long-axis case, and papillary muscles in the short-axis case (arrowheads in the x-t plots in Fig. 3). LLR showed considerable edge blurring. FD produced stair-case artifacts. k-t SLR produced less FD-related artifacts but more edge blurring than LLR + FD. At 10 spokes per time frame, the characteristic artifacts of each method described above were more pronounced. LLR + FD reconstruction more reliably preserved the motion of myocardium than FD reconstruction and provided sharper myocardial border than LLR and k-t SLR.

For all six datasets, smaller regularization weights were observed in the proposed LLR + FD scheme in comparison to using LLR or FD constraint individually. For example, with one dataset (undersampled with the Cartesian golden-angle radial sampling, 10 spokes per time frame), the NRMSE optimal λ_{FD} was 0.01 (NRMSE = 0.109), λ_{LLR} was
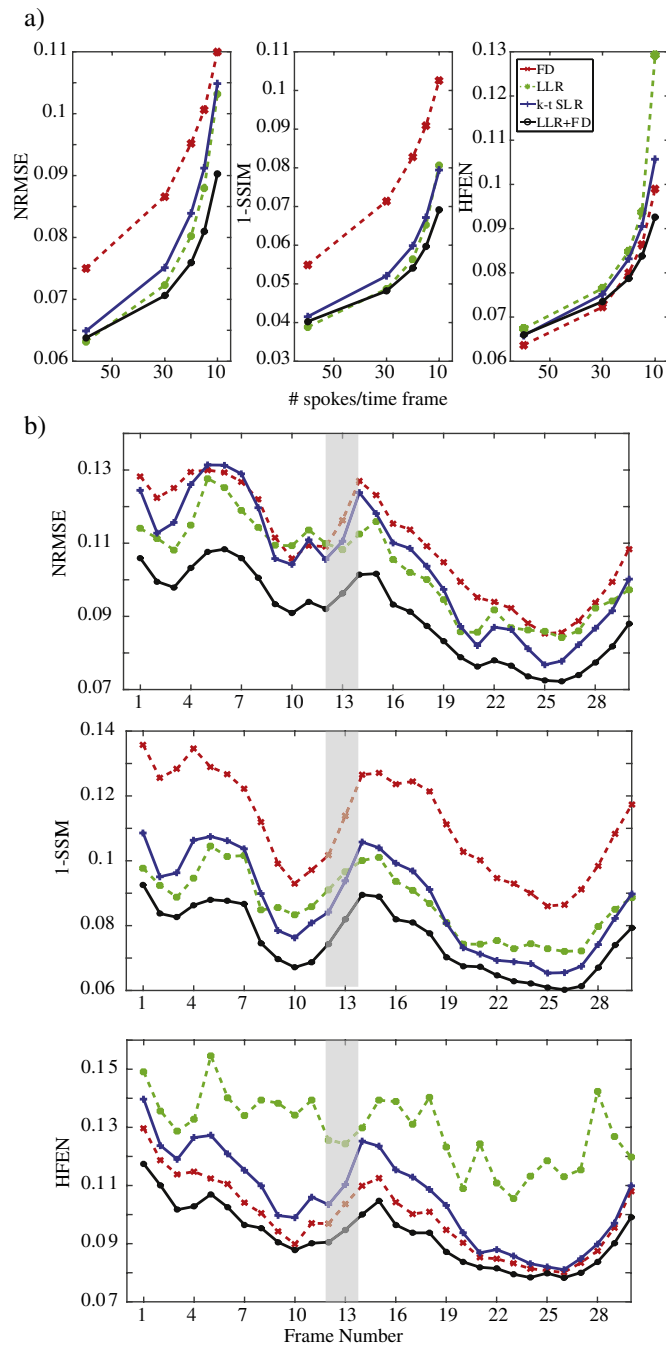
Fig. 2. Quantitative evaluation of one representative dataset undersampled with the Cartesian golden-angle radial sampling pattern. (a) NRMSE, 1-SSIM and HFEN as a function of undersampling level shows consistently superior performance of LLR + FD. (b) Metric versus frame number. The dataset was undersampled with 10 spokes per time frame. The score difference for individual time frames was consistent with the average of the entire time series. The gray area indicates end of systole. Note that 1-SSIM is displayed, so that "lower is better" for all three metrics.

0.3 (NRMSE = 0.103). For LLR + FD, λ_{FD} and λ_{LLR} were 0.006 and 0.06 respectively, and resulted in a higher fidelity reconstruction (NRMSE = 0.0902). This indicates that the FD and LLR constraints are complementary to one another.

Computational burden was significantly reduced by utilizing the twice-variable-splitting ADMM algorithm, which decouples the problem into single-step updates. For all 2D cardiac cine datasets, a six to seven fold reduction in reconstruction time was observed with the ADMM algorithm compared to the penalty-based approach used in previous k-t SLR studies [15,22]. Total reconstruction time using the ADMM approach was 7.8 ± 0.6 min for LLR + FD (parallel

computing applied), and 5.1 ± 0.5 min for k-t SLR. In contrast, 50 min was required with the penalty algorithm for k-t SLR and LLR + FD reconstructions.

4.2. Prospective study

Fig. 4 compares the reconstructions for two prospectively undersampled golden-angle radial datasets. Representative frames from end-systole (ES), end-diastole (ED), and pixel-time profiles are shown. Reference data, obtained using breath-held fully-sampled Cartesian acquisition, provided excellent SNR and contrast. The
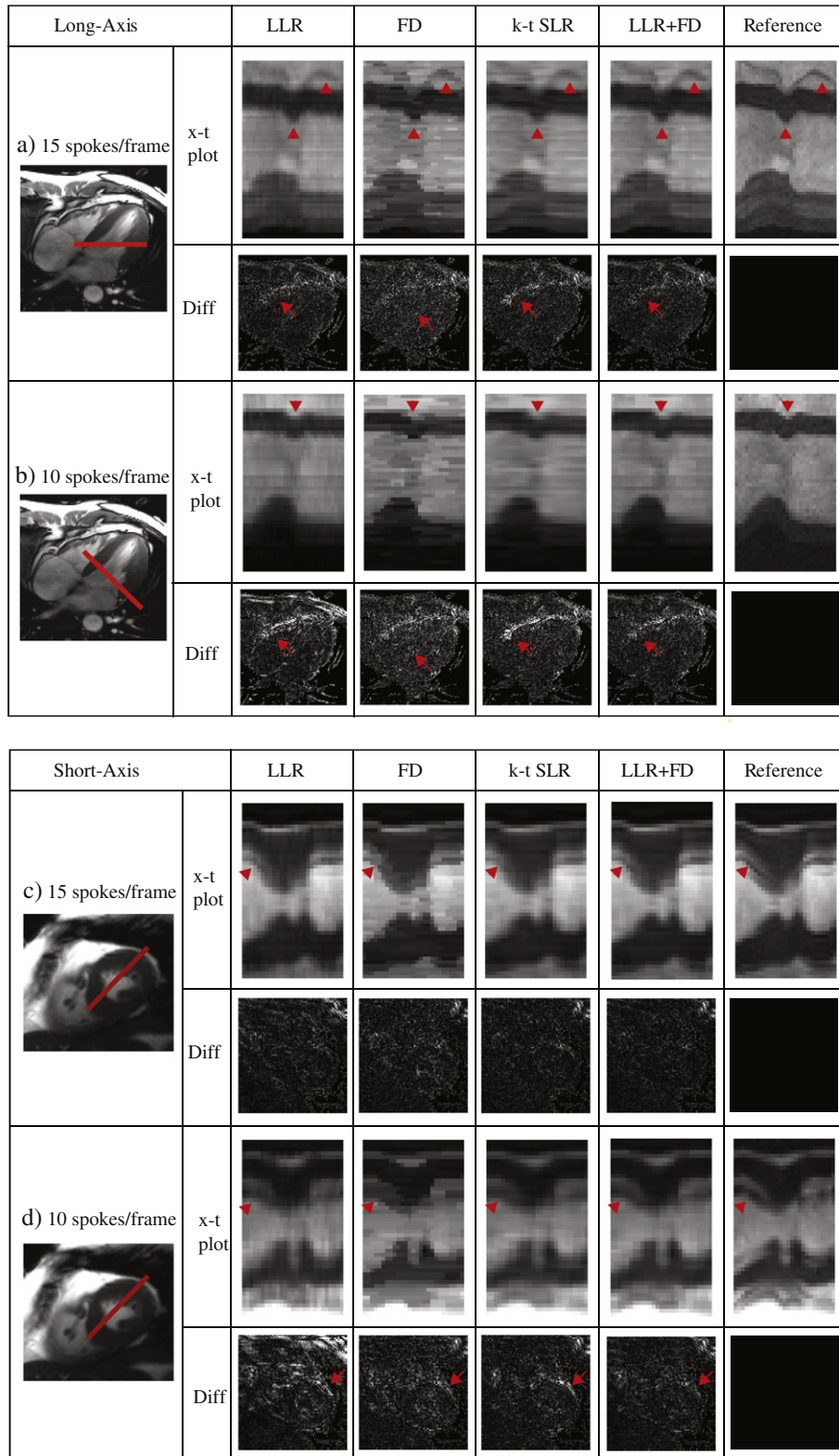
Fig. 3. Qualitative comparison is shown for the four reconstruction methods − LLR, FD, LLR + FD and k-t SLR. Representative long-axis (a and b) and short-axis (c and d) datasets were retrospectively undersampled with Cartesian golden-angle radial pattern at 15 spokes/frame (a and c) and 10 spokes/frame (b and d). x-t plots show the temporal profile of pixels along the red lines in the reference images. Images in end-systole (ES) phase are chosen to show the difference between reconstructed and truth images. Difference images are amplified 6 times for better visualization. In all x-t plots, LLR shows considerable edge blurring. Temporal FD produces stair-case artifact. K-t SLR produces more edge blurring than LLR + FD. Compared to the three other methods, LLR + FD better reconstructed the motion of fine structure such as the tricuspid valve and papillary muscles (arrowheads in x-t plots). In the difference images, LLR and k-t SLR has higher structured error in the ventricle wall indicating more edge blurring than LLR + FD. Temporal FD has less structured error but has more distributed noise in the blood pool.
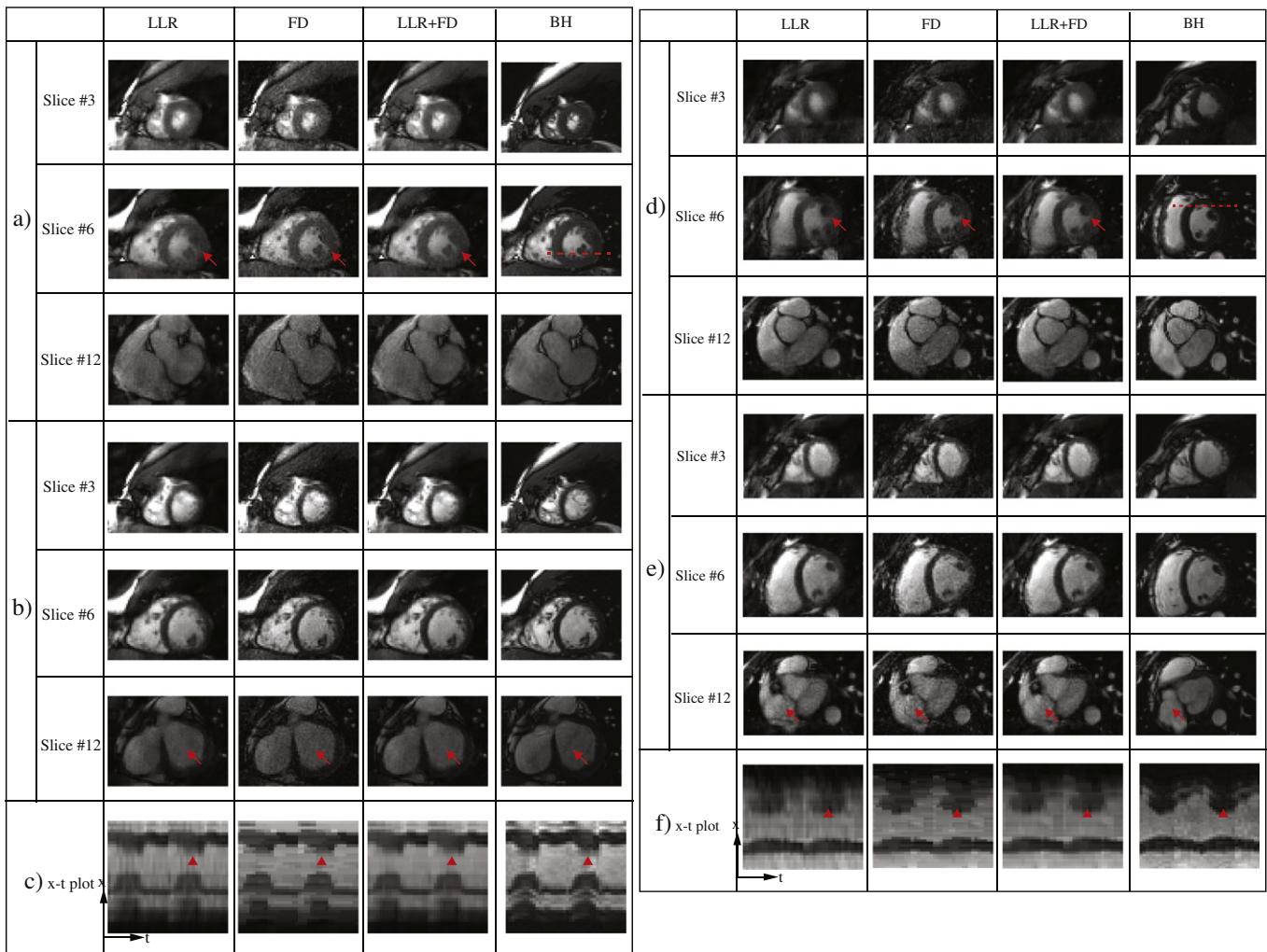
Fig. 4. Results for two prospectively undersampled golden-angle radial datasets. Slices from apex to base in systole (a and d) and diastole (b and e) are shown for three reconstruction methods: LLR, FD, and LLR + FD. Fully-sampled breath-held Cartesian images acquired from the same subject are shown as reference. Pixel-time profiles (c and f) are repeated twice in temporal dimension for illustration, and they show the temporal variation of pixels along the dotted line in slice #6. In both datasets, LLR + FD produced fewer temporal fluctuations and sharper tissue boundary depiction than LLR, and LLR + FD produced fewer stair-case artifacts and less noise than FD (see arrows).

radial datasets were undersampled with 11–13 full spokes per time frame. Compared with the reference scan, LLR + FD most reliably depicted the motion of myocardium. Compared to FD, LLR + FD suppressed temporal stair-case artifact. Compared to LLR, LLR + FD provided sharper edges and less temporal fluctuation due to aliasing.

5. Discussion and conclusions

In this study, LLR + FD was compared against the use of either the temporal FD or the LLR constraint alone. It was found that

LLR + FD provided more natural depiction of myocardial motion compared to FD and improved the depiction of fine structures compared to LLR. Table 1 showed the complimentary strengths of the sparsity and locally low rank constraints. FD was superior in reconstructing edges, as indicated by its high HFEN-ranking, but produced stair-case artifacts at high undersampling levels due to over-regularization. LLR faithfully reconstructed the motion of the myocardium, but produced excessive edge blurring, corresponding to a high SSIM-ranking but low HFEN-ranking. LLR + FD combined the two constraints to produce fewer model-related artifacts with

Table 1

Metric values and ordinal ranking averaged across six datasets are shown for the four reconstruction methods: FD, LLR, k-t SLR, and LLR + FD. The datasets were retrospectively undersampled with Cartesian golden-angle radial sampling at 15 spokes per time frame. Ordinal ranking was based on 1 = best, 4 = worst. FD has lower HFEN indicating its superior performance in reconstructing edges, while LLR faithfully reconstructed the motion of the myocardium, but produced excessive edge blurring, corresponding to a high SSIM but a low HFEN ranking. LLR + FD combining the advantages of LLR and FD achieved the best ranking in all three metrics.

Metrics		FD	LLR	k-t SLR	LLR + FD
NRMSE	Value (%)	8.3	7.4	7.3	**6.7**
	Ordinal Ranking	4.0	2.7	2.2	**1.0**
1-SSIM	Value (%)	8.2	**6.0**	6.2	**5.5**
	Ordinal Ranking	4.0	**2.5**	2.5	**1.0**
HFEN	Value (%)	**9.4**	10.6	9.0	**9.0**
	Ordinal Ranking	**2.7**	4.0	1.7	**1.5**

lower regularization weights for each constraint. Our work shares similarities with a recent work in [33], where the sparsity constraint has been explored in a "local" PSF framework, in which the PSF model order was varied for cardiac and non-cardiac regions. The PSF-based method requires training data and specific sampling scheme for the purpose of computing the temporal basis functions. In comparison, the proposed method does not require the training step but has increased computational complexity.

In the retrospective study, it was observed that LLR + FD more faithfully reconstructed the dynamics of fine structures (e.g. the tricuspid valve in the long-axis view dataset, arrowheads in Fig. 3a) than k-t SLR. This suggests that LLR could be a more appropriate model for cardiac cine images than global low rank. LLR + FD has greater computational complexity because it forces low rank constraints on multiple patch matrices instead of one global matrix. However, in this work, we have observed that the use of parallel computing provides similar computational times with LLR + FD and k-t SLR. It should also be noted that the implementation of k-t SLR in this work exploited the computational benefits due to the splitting of coil sensitivity encoding from the Fourier-undersampling operation in the data consistency term (Appendix A, Eq. (A.1)). This splitting was not considered in the earlier implementation of k-t SLR [15,22], which involved solving an iterative conjugate gradient algorithm to update the reconstruction, and therefore was substantially slower than the splitting strategy considered in this work.

Cartesian golden-angle radial and 2D variable-density random sampling patterns were used in the retrospective study. These two sampling patterns produce incoherent aliasing in the two phase-encoding directions, which was successfully resolved by LLR-based reconstruction methods. We have also evaluated LLR-constrained reconstruction with 1D undersampling cases (not shown), where the variable-density random sampling pattern was applied along a single phase-encoding direction. In these cases, LLR-based methods failed to eliminate residual aliasing. One possible reason is that the Schatten p-norm or nuclear norm minimization, which is often used to force the LLR constraint, requires more sampling incoherence than the 1D sampling scheme can provide.

Based on results in the retrospective study, a golden angle radial sampling was used in a prospective experiment to enable acquisition of multiple 2D slices in a single breath hold. The results may also translate to improving 3D Cartesian acquisition using variable density type sampling patterns in the ky-kz plane [34]. In the prospective study, LLR + FD reconstructions with 2D radial sampling patterns demonstrated improved image quality over either FD or LLR. The FD images appear to provide sharper edges than the LLR + FD reconstructions. However, the FD pixel-time profiles contain significant temporal stair-case artifacts, which include discontinuities that are not physically realistic. It should be noted that LLR + FD reconstructions still contained spatio-temporal blurring, when compared with the Cartesian reference images. Possible reasons could be that (a) the large golden-angle increment in combination with bSSFP may lead to eddy current induced image artifacts from rapidly changing gradients [35] and (b) radial acquisition is more vulnerable to blurring caused by off-resonance and eddy-current effects compared to Cartesian acquisition. Image quality may be further improved by considering (a) small golden-angle radial sampling to reduce eddy-current induced artifacts [36] (b) estimating motion models within the LLR + FD reconstruction to further improve spatio-temporal fidelity [37,38].

Clinical assessment of the artifacts and image quality provided by different reconstruction methods, and their impact on cardiac functional parameters were not performed in this work. Such a study would require a cohort of large number of patient datasets and careful supervision of cardiologists, and is a scope of our future work.

Acknowledgments

Appendix A

An ADMM approach [29] was implemented to solve the optimization problem in Eq. (4). Variable-splitting was performed twice. First, $Z = \Gamma, V_1 = \Phi(Z)$ and $V_2 = \nabla_t(Z)$ are set to split the patch-based operation $\Phi(\cdot)$ and the finite difference operation $\nabla_t(\cdot)$ from the respective norms. Then $U = S \cdot \Gamma$ is set to separate the sensitivity map term from the Fourier sampling term. This splitting avoids the need for an iterative conjugate gradient solver inside each iteration. Eq. (4) was reformulated as:

$$\Gamma^* = \arg\min_{\Gamma} \|F \cdot U - m\|_2^2 + \lambda_{LLR}\|V_1\|_p + \lambda_{FD}\|V_2\|_1,$$
$$\text{subject to } U = S \cdot \Gamma, \; Z = \Gamma, \; V_1 = \Phi(Z), \; V_2 = \nabla_t(Z) \tag{A.1}$$

To solve Eq. (A.1), a Lagrangian functional was formed as:

$$\mathfrak{J}_{\rho_1,\rho_2,\rho_3}(\Gamma, U, Z, V_1, V_1, e_{11}, e_{12}, e_2, e_3)$$
$$= \|F \cdot U - m\|_2^2 + \lambda_{LLR}\|V_1\|_p + \lambda_{FD}\|V_2\|_1 + \dots$$
$$+ \rho_1\|\Phi(Z) - V_1 - e_{11}\|_2^2 + \rho_1\|\nabla_t(Z) - V_2 - e_{12}\|_2^2 + \dots \tag{A.2}$$
$$+ \rho_2\|S \cdot \Gamma - U - e_2\|_2^2 + \rho_3\|\Gamma - Z - e_3\|_2^2$$

e_{11}, e_{12}, e_2 and e_3 are residual variables that would be updated in each iteration. From our experience, ρ_1 and ρ_2 influence the speed of convergence, but have minimal impact on the final reconstruction result. In this work, ρ_2 and ρ_3 were empirically set to 0.05 for all datasets. Eq. (A.2) is solved by alternatively updating each variable, while keeping the other variables fixed resulting in the pseudocode:

- *maxItr* — Stopping criteria by number of iterations (default = 100);
- ρ_1, ρ_2, ρ_3 — Default = 0.05;

While ($n <$ *maxItr*) {

1) Γ –subproblem is solved analytically.

$$\Gamma^{(n+1)} = \arg\min_{\Gamma} \rho_2\left\|S \cdot \Gamma - U^{(n)} - e_2^{(n)}\right\|_2^2 + \rho3\left\|\Gamma - Z^{(n)} - e_3^{(n)}\right\|_2^2$$
$$= \left(\rho_2 S^H S + \rho_3 I\right)^{-1}\left[\rho_2 S^H\left(U^{(n)} + e_2^{(n)}\right) + \rho3\left(Z^{(n)} + e_3^{(n)}\right)\right]$$

2) U –subproblem is solved analytically.

$$U^{(n+1)} = \arg\min_{U} \|F \cdot U - m\|_2^2 + \rho_2\left\|S \cdot \Gamma^{(n+1)} - U - e_2^{(n)}\right\|_2^2$$
$$= \left(F^H F + \rho_2 I\right)^{-1}\left[F^H m + \rho_2\left(S \cdot \Gamma^{(n+1)} - e_2^{(n)}\right)\right]$$

3) Z-subproblem is solved analytically.

$$Z^{(n+1)} = \arg\min_{Z} \rho_1\left\|C_b(Z) - V_1^{(n)} - e_{11}^{(n)}\right\|_2^2 + \rho_1\left\|\nabla_t(Z) - V_2^{(n)} - e_{12}^{(n)}\right\|_2^2$$
$$+ \rho_3\left\|\Gamma^{(n+1)} - Z - e_3^{(n)}\right\|_2^2$$
$$= \left(\rho_1 I + \rho_1 \nabla_t^H \nabla_t + \rho_3 I\right)^{-1}\left[\rho_1\left(V_1^{(n)} + e_{11}^{(n)}\right) + \rho_1 \nabla_t^H\left(V_2^{(n)} + e_{12}^{(n)}\right)\right.$$
$$\left. + \rho_3\left(\Gamma^{(n+1)} - e_3^{(n)}\right)\right]$$

4) V_1-subproblem enforces the LLR constraint. Singular value thresholding is performed on each patch matrix. Patches are recombined after thresholding.

$$V_1^{(n+1)} = \arg\min_{V_1} \lambda_{LLR} \|V_1\|_p + \rho_1 \left\| C_b\left(Z^{(n+1)}\right) - V_1 - e_{11}^{(n)} \right\|_2^2$$
$$= \text{Singular Value thresholding}_{b \in \Omega}\left(C_b\left(Z^{(n+1)}\right) - e_{11}^{(n)} \right)$$

5) V_2-subproblem enforces the temporal FD constraint.

$$V_2^{(n+1)} = \arg\min_{V_1} \lambda_{FD} \|V_2\|_1 + \rho_1 \left\| \nabla_t\left(Z^{(n+1)}\right) - V_2 - e_{12}^{(n)} \right\|_2^2$$
$$= shrink\left\{ \nabla_t\left(Z^{(n+1)}\right) - e_{12}^{(n)} ; \lambda_{FD}/\rho_1 \right\}$$

Shrinkage is computed as:

$$shrink(x, \lambda) = sign(x) \max(|x| - \lambda, 0)$$

6) Update residual variables

$$e_{11}^{(n+1)} = e_{11}^{(n)} - \left(\sum_{b \in \Omega} C_b Z^{(n+1)} - V_1^{(n+1)} \right)$$
$$e_{12}^{(n+1)} = e_{12}^{(n)} - \left[\nabla_t\left(Z^{(n+1)}\right) - V_2^{(n+1)} \right]$$
$$e_2^{(n+1)} = e_2^{(n)} - \left(S \cdot \Gamma^{(n+1)} - U^{(n+1)} \right)$$
$$e_3^{(n+1)} = e_3^{(n)} - \left(\Gamma^{(n+1)} - Z^{(n+1)} \right)$$

}

The implementation of the proposed algorithm using MATLAB can be found at http://mrel.usc.edu/sharing/LLR_TV_ADMM_codes.zip.

References

[1] Kramer CM, Barkhausen J, Flamm SD, Kim RJ, Nagel E. Standardized cardiovascular magnetic resonance (CMR) protocols 2013 update. J Cardiovasc Magn Reson 2013;15:91. http://dx.doi.org/10.1186/1532-429X-15-91.

[2] Hudsmith LE, Petersen SE, Francis JM, Robson MD, Neubauer S. Normal human left and right ventricular and left atrial dimensions using steady state free precession magnetic resonance imaging. J Cardiovasc Magn Reson 2005;7:775–82.

[3] Hunold P, Maderwald S, Ladd ME, Jellus V, Barkhausen J. Parallel acquisition techniques in cardiac cine magnetic resonance imaging using TrueFISP sequences: comparison of image quality and artifacts. J Magn Reson Imaging 2004;20:506–11. http://dx.doi.org/10.1002/jmri.20125.

[4] Wintersperger BJ, Reeder SB, Nikolaou K, Dietrich O, Huber A, Greiser A, et al. Cardiac CINE MR imaging with a 32-channel cardiac coil and parallel imaging: impact of acceleration factors on image quality and volumetric accuracy. J Magn Reson Imaging 2006;23:222–7. http://dx.doi.org/10.1002/jmri.20484.

[5] Lustig M, Santos JM, Donoho DL, JM Pauly. kt SPARSE: high frame rate dynamic MRI exploiting spatio-temporal sparsity. Proc Int Symp Magn Reson Med; 2006. p. 2420.

[6] Lustig M, Donoho D, JM Pauly. Sparse MRI: the application of compressed sensing for rapid MR imaging. Magn Reson Med 2007;58:1182–95. http://dx.doi.org/10.1002/mrm.21391.

[7] Jung H, Sung K, Nayak KS, EY Kim. k-t FOCUSS: a general compressed sensing framework for high resolution dynamic MRI. Magn Reson Med 2009;61:103–16. http://dx.doi.org/10.1002/mrm.21757.

[8] Jung H, Park J, Yoo J, Ye JC. Radial k-t FOCUSS for high-resolution cardiac cine MRI. Magn Reson Med 2010;63:68–78.

[9] Gamper U, Boesiger P, Kozerke S. Compressed sensing in dynamic MRI. Magn Reson Med 2008;59:365–73. http://dx.doi.org/10.1002/mrm.21477.

[10] Feng L, Srichai MB, Lim RP, Harrison A, King W, Adluru G, et al. Highly accelerated real-time cardiac cine MRI using k–t SPARSE-SENSE. Magn Reson Med 2013;70:64–74.

[11] ZP Liang. Spatiotemporal imaging with partially separable functions. ISBI 2007:988–91. http://dx.doi.org/10.1109/ISBI.2007.357020.

[12] Pedersen H, Kozerke S, Ringgaard S, Nehrke K, WY Kim. k-t PCA: temporally constrained k-t BLAST reconstruction using principal component analysis. Magn Reson Med 2009;62:706–16. http://dx.doi.org/10.1002/mrm.22052.

[13] Haldar JP, Hernando D. Rank-constrained solutions to linear matrix equations using power factorization. Signal Process Lett IEEE 2009;16:584–7.

[14] Haldar JP, ZP Liang. Spatiotemporal imaging with partially separable functions: a matrix recovery approach. ISBI 2010:716–9. http://dx.doi.org/10.1109/ISBI.2010.5490076.

[15] Lingala SG, Hu Y, DiBella E, Jacob M. Accelerated dynamic MRI exploiting sparsity and low-rank structure: k-t SLR. IEEE Trans Med Imaging 2011;30:1042–54. http://dx.doi.org/10.1109/TMI.2010.2100850.

[16] Majumdar A. Improved dynamic MRI reconstruction by exploiting sparsity and rank-deficiency. Magn Reson Imaging 2013;31(5):789–95. http://dx.doi.org/10.1016/j.mri.2012.10.026.

[17] Majumdar A, Ward RK, Aboulnasr T. Non-convex algorithm for sparse and low-rank recovery: application to dynamic MRI reconstruction. Magn Reson Imaging 2013;31(3):448–55. http://dx.doi.org/10.1016/j.mri.2012.08.011.

[18] Lingala SG, Jacob M. Blind compressive sensing dynamic MRI. IEEE Trans 2013;32:1132–45.

[19] Trzasko J, Manduca A, Borisch E. Local versus global low-rank promotion in dynamic MRI series reconstruction. Proc Int Symp Magn Reson Med; 2011. p. 4371.

[20] Vitanis V, Manka R, Giese D, Pedersen H, Plein S, Boesiger P, et al. High resolution three-dimensional cardiac perfusion imaging using compartment-based k-t principal component analysis. Magn Reson Med 2011;65:575–87. http://dx.doi.org/10.1002/mrm.22620.

[21] Zhao B, Haldar JP, Christodoulou AG, Liang Z-P. Image reconstruction from highly undersampled -space data with joint partial separability and sparsity constraints. IEEE Trans Med Imaging 2012;31:1809–20. http://dx.doi.org/10.1109/TMI.2012.2203921.

[22] Lingala SG, DiBella E, Adluru G, McGann C, Jacob M. Accelerating free breathing myocardial perfusion MRI using multi coil radial k − t SLR. Phys Med Biol 2013;58:7309. http://dx.doi.org/10.1088/0031-9155/58/20/7309.

[23] Majumdar A, Ward RK. An algorithm for sparse MRI reconstruction by Schatten p-norm minimization. Magn Reson Imaging 2011;29(3):408–17. http://dx.doi.org/10.1016/j.mri.2010.09.001.

[24] Majumdar A, Ward RK. Some empirical advances in matrix completion. Signal Process 2011;91(5):1334–8. http://dx.doi.org/10.1016/j.sigpro.2010.12.005.

[25] Winkelmann S, Schaeffter T, Koehler T, Eggers H, Doessel O. An optimal radial profile order based on the golden ratio for time-resolved MRI. IEEE Trans Med Imaging 2007;26:68–76. http://dx.doi.org/10.1109/TMI.2006.885337.

[26] Haider CR, Hu HH, Campeau NG, Huston J, Riederer SJ. 3D high temporal and spatial resolution contrast-enhanced MR angiography of the whole brain. Magn Reson Med 2008;60:749–60. http://dx.doi.org/10.1002/mrm.21675.

[27] Zhu Y, Guo Y, Lingala SG, Lebel RM, Law M, Nayak KS. GOCART: GOlden-angle CArtesian randomized time-resolved 3D MRI. Magn Reson Imaging 2015;19.

[28] Uecker M, Lai P, Murphy MJ, Virtue P, Elad M, Pauly JM, et al. ESPIRiT — an eigenvalue approach to autocalibrating parallel MRI: where SENSE meets GRAPPA. Magn Reson Med 2014;71:990–1001. http://dx.doi.org/10.1002/mrm.24751.

[29] Ramani S, Fessler JA. Parallel MR Image reconstruction using augmented Lagrangian methods. IEEE Trans Med Imaging 2011;30:694–706. http://dx.doi.org/10.1109/TMI.2010.2093536.

[30] Wang Z, Bovik A, Sheikh HR, Simoncelli EP. Image quality assessment: from error visibility to structural similarity. IEEE Trans Image Process 2004;13:600–12. http://dx.doi.org/10.1109/TIP.2003.819861.

[31] Ravishankar S, Bresler Y. MR image reconstruction from highly undersampled k-space data by dictionary learning. IEEE Trans Med Imaging 2011;30:1028–41. http://dx.doi.org/10.1109/TMI.2010.2090538.

[32] Fessler JA. On NUFFT-based gridding for non-Cartesian MRI. J Magn Reson 2007;188:191–5.

[33] Christodoulou AG, Zhang H, Zhao B, Hitchens TK, Ho C, Liang Z-P. High-resolution cardiovascular MRI by integrating parallel imaging with low-rank and sparse modeling. Biomed Eng IEEE Trans 2013;60:3083–92.

[34] Kim YC, KS Nayak. Free-breathing cardiac 3D cine MRI at 3 T using golden-ratio Cartesian radial sampling and variable flip angle. Proc Int Symp Magn Reson Med; 2014. p. 4364.

[35] Bieri O, Markl M, Scheffler K. Analysis and compensation of eddy currents in balanced SSFP. Magn Reson Med 2005;54(1):129–37. http://dx.doi.org/10.1002/mrm.20527.

[36] Wundrak S, Paul J, Ulrici J, Hell E, Rasche V. A small surrogate for the golden angle in time-resolved radial MRI based on generalized fibonacci sequences. IEEE Trans Med Imaging 2015;34(6):1262–9. http://dx.doi.org/10.1109/TMI.2014.2382572.

[37] Du H, Lam F. Compressed sensing MR image reconstruction using a motion-compensated reference. Magn Reson Imaging 2012 Sep 30;30(7):954–63. http://dx.doi.org/10.1016/j.mri.2012.03.005.

[38] Lingala SG, DiBella E, Jacob M. Deformation corrected compressed sensing (DC-CS): a novel framework for accelerated dynamic MRI. IEEE Trans Med Imaging 2015;34(1):72–85. http://dx.doi.org/10.1109/TMI.2014.2343953.

[39] http://www.ismrm.org/challenge